



Influence of Diluent Concentration in Localized High Concentration Electrolytes: Elucidation of Hidden Diluent-Li⁺ Interactions and Li⁺ Transport Mechanism

Journal:	<i>Journal of Materials Chemistry A</i>
Manuscript ID	TA-ART-06-2021-004737.R2
Article Type:	Paper
Date Submitted by the Author:	23-Jul-2021
Complete List of Authors:	Perez-Beltran, Saul; Texas AandM University, Chemical Engineering Cao, Xia; Pacific Northwest National Laboratory, Energy and Environment Directorate Zhang, Ji-Guang; Pacific Northwest National Laboratory, El-Khoury, Patrick; Pacific Northwest National Laboratory, Chemical Physics & Analysis Balbuena, Perla; Texas AandM University, Chemical Engineering

Influence of Diluent Concentration in Localized High Concentration Electrolytes: Elucidation of Hidden Diluent-Li⁺ Interactions and Li⁺ Transport Mechanism

Saul Perez Beltran¹, Xia Cao⁴, Ji-Guang Zhang⁴, Patrick Z. El-Khoury⁴, and Perla B. Balbuena^{1,2,3,*}

¹Department of Chemical Engineering, ²Department of Materials Science and Engineering, and ³Department of Chemistry, Texas A&M University, College Station, Texas 77843, United States

⁴Energy and Environment Directorate, Pacific Northwest National Laboratory (PNNL), Richland, Washington 99354, United States

*e-mail: balbuena@tamu.edu

Abstract

Localized high concentration electrolytes (LHCE) offer a viable dilution strategy for high concentration electrolytes (HCE) as the dilution process barely impacts the enhanced reductive/oxidative behavior of the HCE formulation but significantly lowers the overall viscosity and, in most cases, increases the ionic conductivity. On the other hand, experimental studies indicate that fluorinated ether electrolytes such as 1,1,2,2-tetrafluoroethylene 2,2,3,3-tetrafluoropropyl ether (TTE) help grow enhanced passivation layers on Ni-rich NMC cathodes. In this work, we study LHCE formulations based on lithium bis(fluorosulfonyl)imide (LiFSI), dimethyl carbonate (DMC), and TTE as the diluent. We use molecular dynamics methodologies, and Raman spectra measurements, to address to what extent the diluent content impacts the coordination behavior of the aggregated structures in the electrolyte and to evaluate the Li⁺ transport properties under the influence of an external electric field. In contrast to other fluorinated ethers, we find that TTE interacts with Li⁺ via fluorine atoms, partially limiting the DMC-Li⁺ interactions hence altering the Li⁺ solvation coordination. This competitive interaction with Li⁺ between the organic solvent and the TTE diluent influences the electrolyte's reductive/oxidative behavior. Nevertheless, the bonding strength of the Li⁺-F_{TTE} is much weaker than those of the Li⁺-O_{DMC} and Li⁺-OFSI⁻. Therefore, the existence of Li⁺-F_{TTE} is in a transient state rather than in a steady state. These results provide plausible guiding rules for future dilution strategies of HCE electrolytes. We also demonstrate that Li⁺ ions drift under the electric field's influence via repeated ion dissociation/association processes following a hopping conduction mechanism. Li⁺ ions jump between aggregated networks where Li-O interactions dominate via diluent-enriched phases, a process in which the solvation shells temporarily

mutate to a Li-F dominated coordination structure. We expect our results to contribute an improved atomic-level understanding of the solvation structure and dynamics of LHCE electrolytes.

Introduction

Modern society's lifestyle exerts constant pressure on pursuing new electrochemical devices with ever longer and higher cycling life and energy density. In this regard, lithium (Li) metal batteries (LMBs) based on lithium metal anodes and Ni-rich layered oxides $\text{LiNi}_x\text{Mn}_y\text{Co}_{1-x-y}\text{O}_2$ (NMC) have surfaced as promising candidates for the next generation of ultra-high energy density batteries.^{1,2} Li metal possesses a high theoretical specific capacity like no other known material (3860 mAh/g) and ultralow electrochemical redox potential (-3.040 V vs. SHE).³ Ni-rich NMC delivers a specific capacity greater than 200 mAh/g with improved high-voltage cyclability (up to 4.7 V vs. Li^+/Li).⁴ However, these two electrode materials are also highly reactive. No conventional electrolyte formulations are stable enough to resist the harsh reducing/oxidizing environment on the electrodes' surfaces in normal battery operation conditions, leading to uncontrollable dendrite growth, continuous electrolyte oxidative decomposition, and other side effects.⁵⁻⁸

Localized high concentration electrolytes (LHCE) constitute a game-changer for ultra-high energy density batteries that shows compatibility with both Li metal and Ni-rich NMC materials.^{6,9} In addition to the typical Li salt and organic solvent, the LHCE electrolyte contains an organic diluent with relatively low permittivity, low donor ability, and wide electrochemical stability window.^{3,6,10-12} The relative high salt/solvent concentration improves the electrolyte reductive/oxidative stability by lowering non-associated organic solvent molecules' availability. The diluent reduces viscosity and enhances the overall wettability on electrodes and separators.³

In LHCE electrolytes, the salt anion should possess a large and flexible molecular structure with multiple coordination sites or "docking stations" to allow aggregation without precipitation. Examples of suitable Li salts are lithium bis(trifluoromethanesulfonyl)imide (LiTFSI) and lithium bis(fluorosulfonyl)imide (LiFSI).⁵ Solvent molecules have similar interaction strength with Li^+ ions than Li salts and they compete with the anion for Li^+ coordination. Organic solvents, either ether-based such as 1,2-dimethoxyethane (DME) or ester-based like dimethyl carbonate (DMC), generally coordinate with a single Li^+ ion.^{6,12,13} On the other side, the diluent barely competes for Li^+ coordination and does not dissociate the Li salt.¹⁰ Fluorinated ethers such as

bis(2,2,2-trifluoroethyl) ether (BTFE) and 1,1,2,2-tetrafluoroethyl 2,2,3,3-tetrafluoropropyl ether (TTE), are believed to act as interface modifiers that improve the formation of fluorinated interphases on both electrodes and suppress undesired solvent decomposition.^{6, 10, 14}

TTE diluent is a fluoroalkyl ether with negligible solvability for the LiFSI salt. This characteristic, coupled with a rare TTE-Li⁺ interaction via ether oxygen atoms, leads to calling the TTE an “inert diluent” that does not interfere with solvation shells in LHCE electrolytes.¹⁵ Reports from LHCE formulations, based on LiFSI, DME, and TTE, indicated enhanced stability of Ni-rich NMC cathodes under high challenging conditions such as high voltage, high-loading cathode, thin Li anode, and lean electrolyte.³ For this electrolyte, ¹⁷O-nuclear magnetic resonance (NMR) measurements indicate that the diluent shields ethereal oxygen atoms from Li⁺ solvation shells as the chemical shift of ethereal oxygen atoms from DME molecules decreases in the LHCE. Besides, X-ray photoelectron spectroscopy (XPS) analyses carried on cycled Ni-rich NMC cathodes show LiF as the major species of the passivation layer, along with a significant C atomic ratio. Even though these results, and other works,⁷ indicate the TTE plays a vital role in the composition of the LiF-enriched passivation layer, there is still a lack of understanding of how the diluent impacts the electrolyte’s aggregated structural features. An increase in the FSI-Li⁺ coordination does not fully explain the shielding effect of ethereal oxygen from the solvation shells.

The electric field-driven Li⁺ ion transport mechanism in LHCE electrolytes differs from the conventional vehicle-type mechanism in dilute electrolytes.^{5, 9, 16} The increase in carrier density changes the ion transport mechanism to a fluid-like viscosity decoupled ion movement that follows a hopping-type ion transport similar to that in inorganic solid electrolytes.¹⁷ Arguably, the elevated salt concentration creates aggregates structures acting as continuous percolating networks with a high density of pseudo-equivalent sites with low barrier energies between adjacent sites for an ion to hop easily from one site to another. However, it is yet unclear if Li⁺ ions move exclusively within these aggregated structures in a type of knock-off or correlated diffusion mechanism due to the increased ion density, as in solid-state electrolytes,¹⁸⁻²⁰ or Li⁺ ions follow a mixed structural/vehicular transport mechanism bouncing between aggregated clusters via rich solvent/diluent phases. Experimental efforts to elucidate this transport mechanism include infrared spectroscopy (IR), conductometric analysis, nuclear magnetic resonance (NMR), and dielectric spectroscopy.¹⁶ However, these methodologies are limited in liquid media even though they are effective in solid media.⁹ Theoretical modeling such as

molecular dynamics fills this gap, offering a better choice for a mechanistic understanding of the ion transport at the atomic level.^{16, 21, 22}

In this work, we characterize to what extent the diluent content interferes with the solvation shells that build up the aggregated structures in LHCE electrolytes made from LiFSI, DMC, and TTE, and elucidate the ion transport mechanism driving Li^+ ions throughout the electrolyte under the presence of an applied electric field. We address these questions using molecular dynamics simulations. We use both ab initio molecular dynamics (AIMD) and classical molecular dynamics (classical MD). First, we perform AIMD calculations to evaluate how the diluent changes the electrolyte solvation structure and compare it with Raman spectra measurements. Second, we add the electric field to the classical MD simulations to address the transport properties under an applied external electric field. We find that TTE interacts with Li^+ via fluorine atoms. Interaction via ether oxygen is negligible. TTE effectively modifies the aggregated liquid structure as both diluent and DMC competitively coordinate with Li^+ , which turns out to change the electrolytes' reductive/oxidative behavior, providing a probable explanation on why TTE plays a role in growing passivation layers in cycled Ni-rich cathodes at high voltages. Finally, we demonstrate that Li^+ drifts under the electric field's influence via repeated ion dissociation/association process following a hopping conduction mechanism. We find that Li^+ ions jump between aggregated networks where Li-O interactions dominate, via diluent-enriched phases, a process in which the solvation shells temporarily mutate to a Li^+ -F dominated coordination structure. We expect our results to contribute to a better atomic-level understanding of the liquid structure of LHCE electrolytes and to provide pathways to novel dilution strategies of high concentration electrolytes (HCE).

Computational and Experimental Details

We used AIMD and classical MD simulations in tandem to elucidate the liquid structure at the atomic level and the Li^+ transport mechanism in a series of LHCE formulations made from mixtures of LiFSI, DMC, and TTE. We also measured Raman spectroscopy for the selected formulations to corroborate our findings. Raman spectra were collected on an inverted optical microscope (Nikon Ti-E) coupled to the Raman spectrometer (LabRam HR, Horiba), using a minimal power of 50 μW from a 633 nm laser source, which was delivered to the samples using a 10X air objective.²³

AIMD Calculations

We use the Vienna ab-initio simulation package (VASP, version 5.44)²⁴⁻²⁶ to run the AIMD simulations and work with simulation cells with periodic boundary conditions along the x-, y-, and z-coordinates. The input geometries are LiFSI, DMC, and TTE molecules packed randomly in the simulation cell using an initial guess for the volumetric density (2.00 g/cm³). We followed a 5 ps long Parrinello-Rahman dynamics calculation (in the NPT ensemble) with the pressure set to 1 atmosphere at 330 K obtaining the equilibrium density after the simulation cell's volume stabilization. Small changes in the density do not largely affect the structural properties. The following set of simulations ran with the NVT ensemble, with each simulation lasting for a least 50 ps. Our earlier work proved this simulation time to be long enough to allow the formation of extended networks of aggregates (AGGs) typical of HCE and LHCE electrolytes.¹² The Langevin thermostat controls the Parrinello-Rahman dynamics' temperature with the Langevin friction coefficients set to 5.0 ps⁻¹ for all atomic species.²⁷⁻²⁹ The friction coefficient and the fictitious mass for the Parrinello-Rahman lattice degrees of freedom are 5.0 ps⁻¹ and 20 amu. For the NVT simulations, temperature control is through the Nose-Hoover thermostat method with the Nose-mass parameter set to 0.5.³⁰⁻³²

All dynamics calculations run with the time step set to 1.2 fs after changing the hydrogen mass to its tritium isotope.³³ The projector-augmented wave (PAW) pseudopotential describes the core-electron dynamics,³⁴ whereas the plane-wave basis set with the energy cutoff set to 300 eV models the valence electrons. The generalized gradient approximation by Perdew-Burke-Ernzerhof (PBE-GGA) describes the exchange-correlation functional,³⁵ and the Monkhorst-Pack scheme set to 1x1x1 performs the Brillouin zone integration.³⁶ Modeling of the partial occupancies is done through the Gaussian smearing method set to 0.05 eV. The convergence criteria for the electronic self-consistent and the ionic relaxation loops are 10⁻⁴ and 10⁻³ eV, respectively.

We extract selected frames from the AIMD-NVT atomic trajectories and perform geometry optimization before calculating the electrolyte's structural and electronic features. For this set of geometry optimizations, the cutoff for the valence electrons' energy changes to 400 eV while all the other simulation parameters remain unchanged.

We use the package local orbital basis suite towards electronic-structure reconstruction (LOBSTER) to calculate the projected density of states (pDOS) and the projected crystal-orbital Hamilton population (pCOHP) analysis.³⁷⁻⁴² The projection calculation uses Bunge's local basis functions, including the 1s orbital for hydrogen, 2s for Li, 2s and 2ps for carbon (C), fluorine (F),

nitrogen (N), and oxygen (O), and 3s and 3p for sulfur (S). The absolute charge spilling remains lower than 1.99% in all cases. Calculation of molecular pDOS profiles includes orbital contributions from each atom. The Bader charge method carries out the electronic charge calculation for each species in the electrolyte.⁴³⁻⁴⁵

Classical Molecular Dynamics Calculations

Classical MD simulations address the ionic transport mechanism of the LHCE electrolyte. We use the classical MD implementation from the large-scale atomic/molecular massively parallel simulation package (LAMMPS, version 3 Mar 2020).⁴⁶ Input geometries for these simulations come from replicating the output geometries from AIMD-NVT simulations along the x-, y-, and z-coordinates. Replication takes advantage of the lower computational cost from using classical MD by creating bigger simulation cells suitable to calculate the electrolyte structure's bulk properties.⁴⁷

First, we perform isothermal equilibration runs for about 500 ps at 330 K with the NVT ensemble, 0.25 fs time step, and Nose-Hoover method for time integration with the damping parameter set to 0.01 fs⁻¹. Production jobs follow and run for another 1000 ps. Periodic boundary conditions apply in all three coordinates, with a 12 Å cutoff for van der Waals (vdW) and Coulombic pairwise interactions.⁴⁷ The intramolecular interactions for the Li⁺ ions and FSI⁻ anions are modeled using the OPLS-AA parameterization,⁴⁸ whereas the ReaxFF parameterization governs the intramolecular interactions for the DMC solvent and TTE diluent molecules.⁴⁹ vdW parameters and partial electronic charges for intermolecular interactions between Li⁺ ions and FSI⁻ anions, and DMC and TTE molecules from other authors' earlier works.^{47, 48, 50} We compare the bulk properties of the liquid electrolyte structure from this set of simulations against the AIMD-NVT calculations to verify the force field parameterization's ability to address the inter/intra-molecule interactions.

We add an external electric field (0.4 V/Å) to address the Li⁺ transport mechanism, for which we replicate further the output geometries from classical MD-NVT simulations along the same direction along which we apply the electric field, providing extra room to follow the drift displacement throughout the bulk liquid structure.

Results

AIMD Calculations

Table 1 shows the molar ratio, number of molecules packed, cell size, volumetric density, and molarity for each of the four formulations simulated in this work. Currently, these formulations are under further research at the Pacific Northwest National Laboratory (PNNL). Five ps of AIMD-NpT simulation proved long enough to allow for volume stabilization showing no significant deviation from the initial guessed density. Electrolyte's molarity averaged over the last picosecond of simulation.

Regardless of the number of packed molecules, the simulation cell sizes are such that no formulation has more than 406 atoms, keeping the computational cost acceptable. The Li-salt vs. solvent molar ratio remains nearly constant in all formulations, within the limitations due to the simulation size. We only vary the diluent content to understand its impact on both the liquid structure and the Li⁺ transport mechanism. Our early work proves that an HCE electrolyte with a LiFSI:DMC molar ratio equal to 1:2, possesses a salt concentration high enough to enhance the electrolyte reductive/oxidative stability compared to the equivalent diluted formulation (1.21 M).¹² From formulations A1 to A4, lowering the TTE content increases electrolyte molarity from 1.35 to 2.79 M.

Table 1: Electrolyte formulations addressed in this work

Electrolyte Formulation	Molar Ratio LiFSI:DMC:TTE	# Molecules LiFSI:DMC:TTE	Unit cell size a1 x a2 x a3 [Å]	Average Molarity [M]
A1	1.00:2.00:5.00	3:6:16	15.47 x 15.59 x 15.23	1.35
A2	1.00:2.16:4.31	4:8:15	15.51 x 15.45 x 15.52	1.77
A3	1.00:2.00:3.00	4:9:13	15.11 x 14.95 x 15.58	1.88
A4	1.00:2.00:2.00	6:11:11	15.07 x 15.15 x 15.65	2.79

Figure 1 (a) and (b) show the partial radial distribution function (PRDF) profiles for the Li-O and Li-F interactions for both the A1 and A4 formulations. The Li-O interactions peak at 1.92 Å, very close to AIMD calculations performed in other works with LiFSI, DMC, and BTFE mixtures,⁶ whereas the Li-F interactions center at 2.14 and 1.99 Å, respectively. The Li-O interaction comes from sulfonyl oxygen atoms from FSI⁻ anions and carbonyl oxygen atoms from DMC molecules, whereas the Li-F profile comes from TTE molecules. The PRDF profiles from our earlier work with LHCE electrolytes with LiFSI, DMC, and BTFE, do not show any significant Li-F interaction despite the presence of FSI⁻ anions. Moreover, earlier works with electrolytes with

TTE as the diluent point out to negligible TTE-Li⁺ interactions via ether oxygen atoms but do not address TTE-Li⁺ coordination via F atoms.^{3, 7} This observation suggests, as we demonstrate later in this work, that Li⁺-F interactions come from the TTE molecules.

The integral of the pCOHP population curves (IpCOHP) adds understanding on the relative strength of the bonding interactions holding together the solvation shells around the Li⁺ ions.^{38, 51} Figure 1 (c) plots, for all formulations, the ICOHP integrals vs. the bonding distances for the interactions Li⁺-O_{FSI}, Li⁺-O_{cbnyl}, and Li⁺-F_{TTE}. The interactions with oxygen atoms (O_{FSI}⁻ and O_{cbnyl}) center on 1.9 Å, and rank the lowest (more negative) values for the ICHOP integral, meaning stronger bonding than F_{TTE} atoms. The bonding distances for the Li-F_{TTE} interactions spread between 1.94 to 2.5 Å. The broad bond distances distribution for the Li-F_{TTE} interactions, suggests more flexibility compared to Li⁺ interaction with oxygen. As shown in a later section, dilution triggers the contribution of Li-F interaction for the solvation shell and strengthens the Li⁺-FSI⁻ interaction. The weaker Li-F interaction suggests the TTE molecules could easily detach from the solvation shell, which in the long term might create chances for a higher FSI coordination. This line of reasoning might explain the salt precipitation observed in experiments for LiFSI:DMC:TTE electrolytes due to TTE over-saturation.⁵²

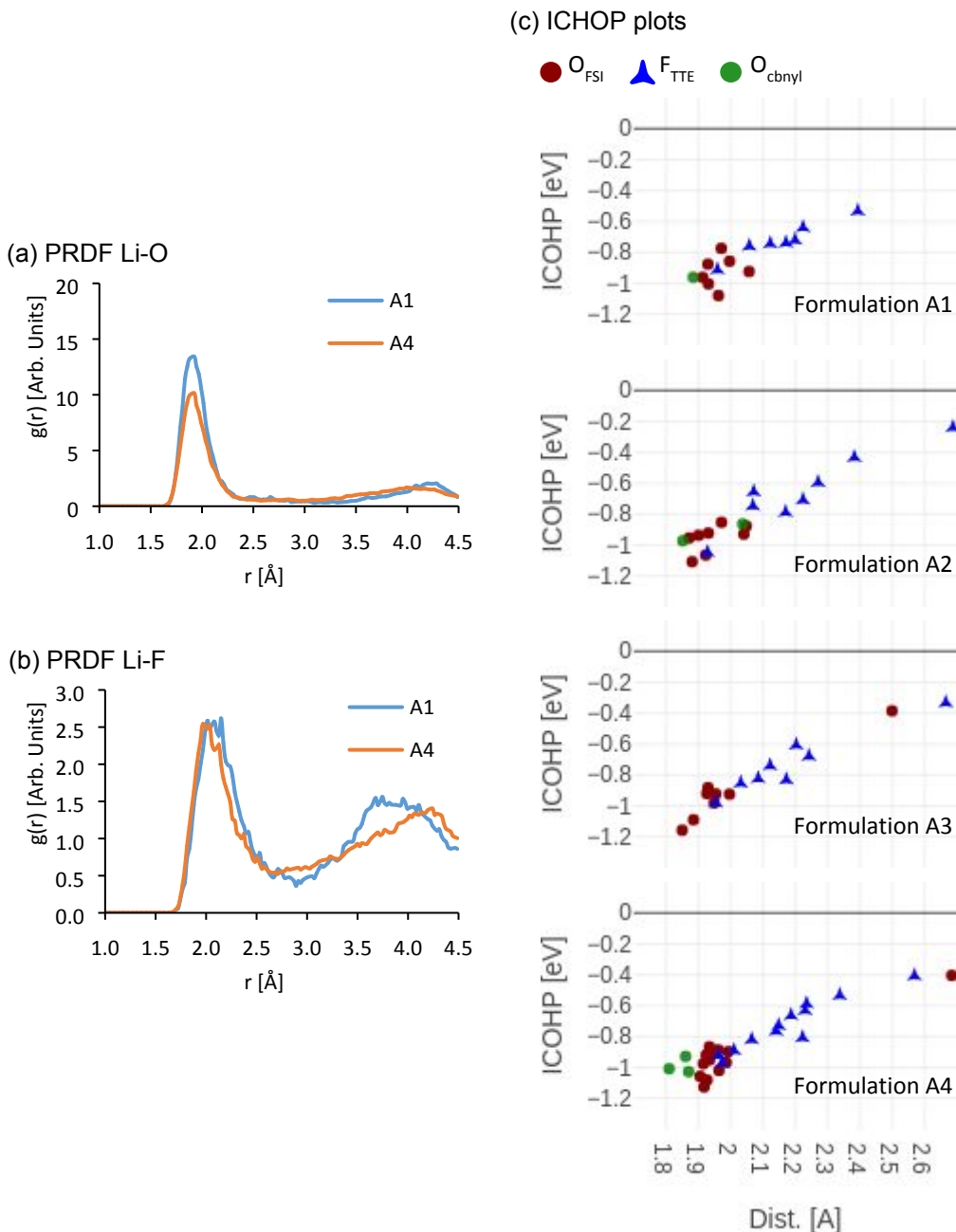


Figure 1: AIMD-NVT partial radial distribution functions (a) Li-O and (b) Li-F for formulations A1 and A4. ICHOP plots for interactions Li⁺-O_{FSI}- (dark red filled dots), Li-FTTE (blue filled triangles), and Li⁺-O_{cbnyl} (green filled dots).

Figure 2 and Figure 3 provide further insight into the nature of the atomic interactions discussed in the above paragraph. Figure 2 (a) plots the global coordination number for each Li⁺ ion (Li⁺ index) packed in the simulation cell for formulation A1, averaged over the last ten ps of the AIMD-NVT simulation. Li⁺ coordination oscillates between 4.5 and 5 atoms, slightly higher than the tetrahedrally coordinated structures formed around Li⁺ ions in dilute and LHCE electrolyte formulations with BTFE as the diluent.^{53, 54} Figure 2(b) breaks down the averaged contributions

to each atomic species' global coordination number average over the last ten ps. The error bars plotted on each value represent the average's standard deviation.

In Figure 2(b), sulfonyl oxygen atoms from FSI⁻ anions (O_{FSI}) and F atoms from TTE molecules (F_{TTE}) contribute the most to complete the solvation shell around Li⁺ ions. The Li⁺- O_{FSI} coordination shows negligible to zero standard deviation. However, the error bars for the Li⁺- F_{TTE} coordination are larger, contributing the most to the standard deviation plotted for the global coordination number in Figure 2(a); we corroborate later in this work that this behavior indicates weaker Li⁺- F_{TTE} interactions compared to Li⁺- O_{FSI} . Li⁺ coordination with carbonyl oxygen atoms from DMC varies from one to no DMC molecule completing the solvation shell. Moreover, the FSI⁻ anions do not coordinate with Li⁺ via F atoms and Li⁺-TTE coordination via ether oxygen (not shown) is zero, in agreement with experimental studies.⁷ This coordination behavior hints that TTE and DMC molecules competitively coordinate with Li⁺ via F and carbonyl oxygen atoms (O_{cbnyl}), respectively.

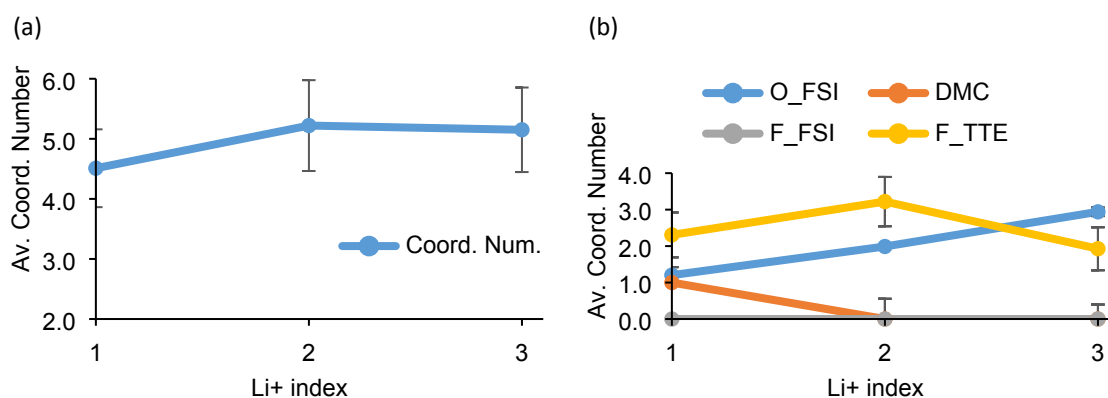


Figure 2: Li⁺ coordination behavior from AIMD-NVT simulations in formulation A1: (a) global coordination number, (b) species contribution to the Li⁺ coordination number. The Li⁺ index labels the Li⁺ ions packed in the simulation cell.

Figure 5 shows the average Li⁺ coordination behavior across all formulations. The Li⁺ ions coordinate five atoms approximately regardless of the TTE concentration. The Li⁺ ions consistently coordinating with at least two sulfonyl oxygen atoms, indicative of CIP and AGGs formation, proper of LHCE electrolytes.⁶ The number of F atoms from TTE molecules adding to the coordination shell ranks close to three at high diluent contents (A1) but lowers down to one with lower diluent content (A4). The average number of DMC molecules completing the Li⁺ solvation shell is lower than one in formulations with high TTE contents such as the formulation A1; evidencing that in some cases only FSI⁻ anions and TTE molecules via F atoms complete

the Li^+ solvation shell. However, this behavior changes with lower diluent contents as the average increases to ~ 1 in formulations A3 and A4.

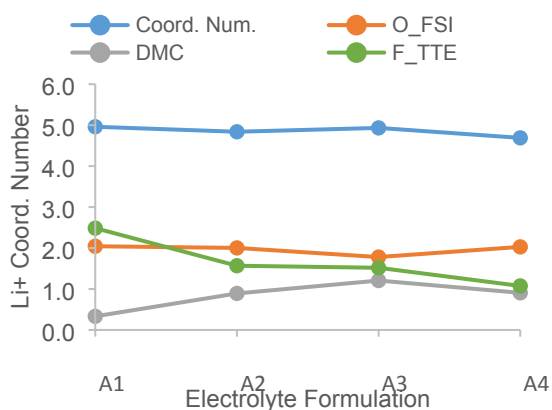


Figure 3: Li^+ coordination behavior based on diluent contents: Global coordination number (Coord. Num.) and species contribution to the coordination number

Figure 4 shows the calculated average number of Li^+ ions interacting with each FSI^- anion, DMC, and TTE molecules across all formulations and compares this information with Raman spectra measurements for A1, A3, and A4, compared with pure DMC and pure TTE. Figure 4 (a) shows that FSI^- anions interact with two Li^+ ions, with no changes in this behavior with the diluent content, meaning that the TTE diluent does not affect the Li^+ - FSI^- coordination. The Raman spectra plotted in Figure 4 (d) corroborates this observation; the peak assigned to FSI^- anions coordinated with Li^+ ($\sim 750 \text{ cm}^{-1}$) only suffers a light intensity attenuation due to dilution from A4 to A1, and instead shifts to the left, proper of a strengthened coordination behavior. Figure 4 (b) shows that TTE molecules engage only one F atom if interacting with a Li^+ ion, and this behavior does not change regardless that the ratio of TTE molecules interacting with Li^+ increases from 40% to 80% as the diluent content decreases, meaning a relatively lower availability of free (non-associated) TTE molecules.

The solvent's coordination behavior shows (Figure 4 (c)) that on average, each DMC molecule interacts with one Li^+ ion only (via the carbonyl oxygen atom). Moreover, the percentage of DMC molecules engaged in Li^+ -O interactions increases from 20% to 60%, going from formulations A1 to A4 (lower diluent contents). This behavior suggests that for high diluent contents, some Li^+ ions complete their solvation shell with FSI^- anions and/or TTE molecules exclusively, leaving some DMC molecules as non-associated solvent molecules embedded within the bulk liquid phase. Raman measurements in Figure 4 (d) show that the free DMC vibration band centered at $\sim 920 \text{ cm}^{-1}$ becomes attenuated across formulations A4 to A1. Moreover, the integral

pCOHP population plots shown in Figure 1c reveal that the Li^+ -F interactions are comparatively much weaker than Li^+ - O_{cbnyl} interactions, suggesting that non-associated DMC molecules exist in this state only for time periods too short before engaging in a Li^+ solvation shell so Raman measurements cannot detect them. However, these weaker Li^+ -F interactions between the cation and the diluent play a role in ionic transport, as discussed in a later section.

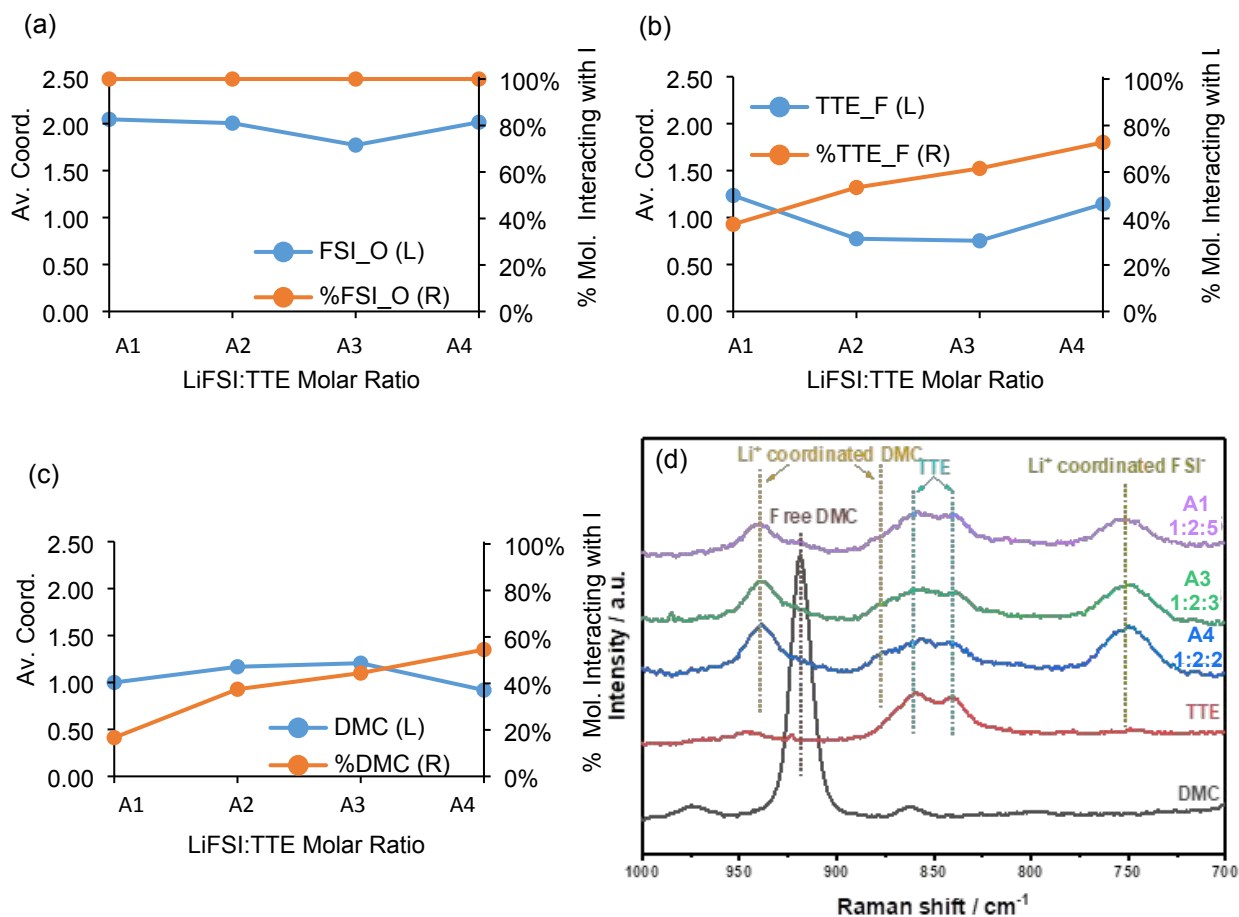


Figure 4: Averaged coordination (left vertical axis, L) and percentage of molecules interacting with Li^+ (right vertical axis, R): (a) FSI⁻ anions, (b) TTE diluent molecules, and (c) DMC solvent molecules, (d) Progression of Raman spectra for pure DMC and TTE, and formulations A1, A3, and A4

Figure 5 (a) shows a grey-colored polyhedral construction around the interconnected solvation shells in high-diluent formulation A1. The DMC and TTE molecules complete the solvation shells that build up this aggregated network, but their inability to engage simultaneously with multiple Li^+ ions limits their ability to grow aggregates. Instead, the aggregates are driven by FSI⁻ anions. Their flexibility to engage with multiple Li^+ ions via sulfonyl oxygen atoms in different configurations gives room to the formation of aggregated networks embedded in the electrolyte liquid structure.¹²

Figure 5 (b) highlights one of the solvation shells embedded in this polyhedral construction, in which the Li^+ interacts with FSI⁻ anions and TTE molecules only. The left column in Figure S1 (supporting information) shows the PRDF profiles from the AIMD-NVT simulations for Li-O and Li-F across all formulations.

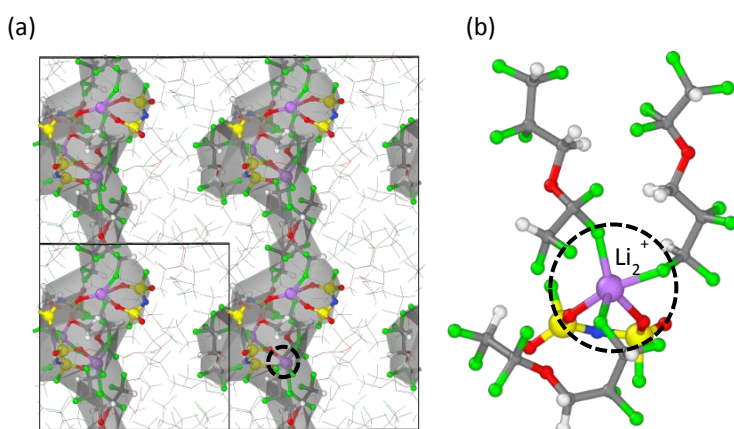


Figure 5: (a) Aggregated networks in formulation A1: grey colored polyhedral construction drawn around the interconnected solvation shells. (b) Detailed view of one of the solvation shells building up the aggregated network structure.

We use a screening level methodology introduced in our earlier work to correlate the electrolyte reductive/oxidative properties manifested in HOMO/LUMO levels to the liquid heterogeneities, Bader electronic charge, and Li^+ coordination behavior.¹² Figure 6 summarizes these calculations performed on selected frames from the AIMD-NVT simulations for all formulations. Note that the reported HOMO/LUMO levels in Figure 6 were extracted from the density of states of the complete cell so they reflect the effects of the electrolyte environment on the electronic distribution of each molecular component. The x- and y-axes in each plot correspond to the Bader electronic charge and LUMO levels, and the left, centered, and right-sided columns present information on the DMC solvent molecules, the FSI⁻ anions, and the TTE diluent molecules, respectively. Each symbol plotted represents an individual molecule or anion. For

the solvent, the pentagons and triangles pertain to DMC molecules that either coordinate or not to a Li^+ ion via carbonyl oxygen atoms.

Meanwhile, the grey-red colored scale bar corresponds to DMC coordination via ester oxygen atoms; grey means no coordination and red means two ester oxygen atoms coordinating to a Li^+ ion. For the FSI^- anions, pentagons and triangles indicate coordination, or not, to Li^+ via a F atom. The rainbow-colored bar refers to coordination via sulfonyl oxygen atoms; dark blue means no coordination and dark red all four oxygen atoms coordinating to Li^+ ions. Finally, symbols for TTE molecules indicate coordination to Li^+ via the ester oxygen atom, while the colored bar symbolizes coordination via F atoms.

Regardless of the electrolyte formulation, the lowest LUMO level falls on an FSI^- anion. Coordination with Li^+ via F atoms is not dominant but lowers the LUMO levels as well. Besides, the tendency to more negative Bader charge values correlates to higher coordination with Li^+ . The more Li^+ ions coordinating to the FSI^- via sulfonyl oxygen atoms, the lower the LUMO level, hence the more likely the anion to reduce.^{12, 14}

DMC molecules coordinating with Li^+ via carbonyl or ester oxygen atoms show lower LUMO levels than free solvent molecules. However, the ratio of free solvent molecules dominates. This behavior differs from our earlier study on $\text{LiFSI}:\text{DMC}$ HCE and LHCE electrolytes with the same $\text{LiFSI}:\text{DMC}$ molar ratio but using BTFE as the diluent, where most of the DMC molecules engaged in interactions with Li^+ ions.¹² The difference here comes from using of TTE. Both TTE and DMC molecules compete to coordinate with Li^+ ions via Li-F or Li-O, respectively.

TTE molecules do not coordinate with Li^+ via ester oxygen atoms. However, the proportion of TTE molecules coordinating via one or even two F atoms is notable and increases with lowering the diluent content. As with FSI^- anions and DMC molecules, coordination with Li^+ lowers the LUMO levels, making the TTE molecule more likely to be reduced.¹⁴ This behavior is particularly evident in formulations A1 and A2 for those TTE molecules coordinating two of their F atoms with Li^+ ions.

In summary, coordination with Li^+ drags electronic charge, hence lowers the LUMO level and makes the anion or molecule more likely to reduce. This effect, coupled to the flexibility of FSI⁻ anion to coordinate with Li^+ via multiple sulfonyl oxygen atoms and to the presence of free DMC solvent molecules, triggered by TTE dilution, explains the electrolyte's tendency to favor Li salt reduction over DMC, leading to a more stable SEI film.

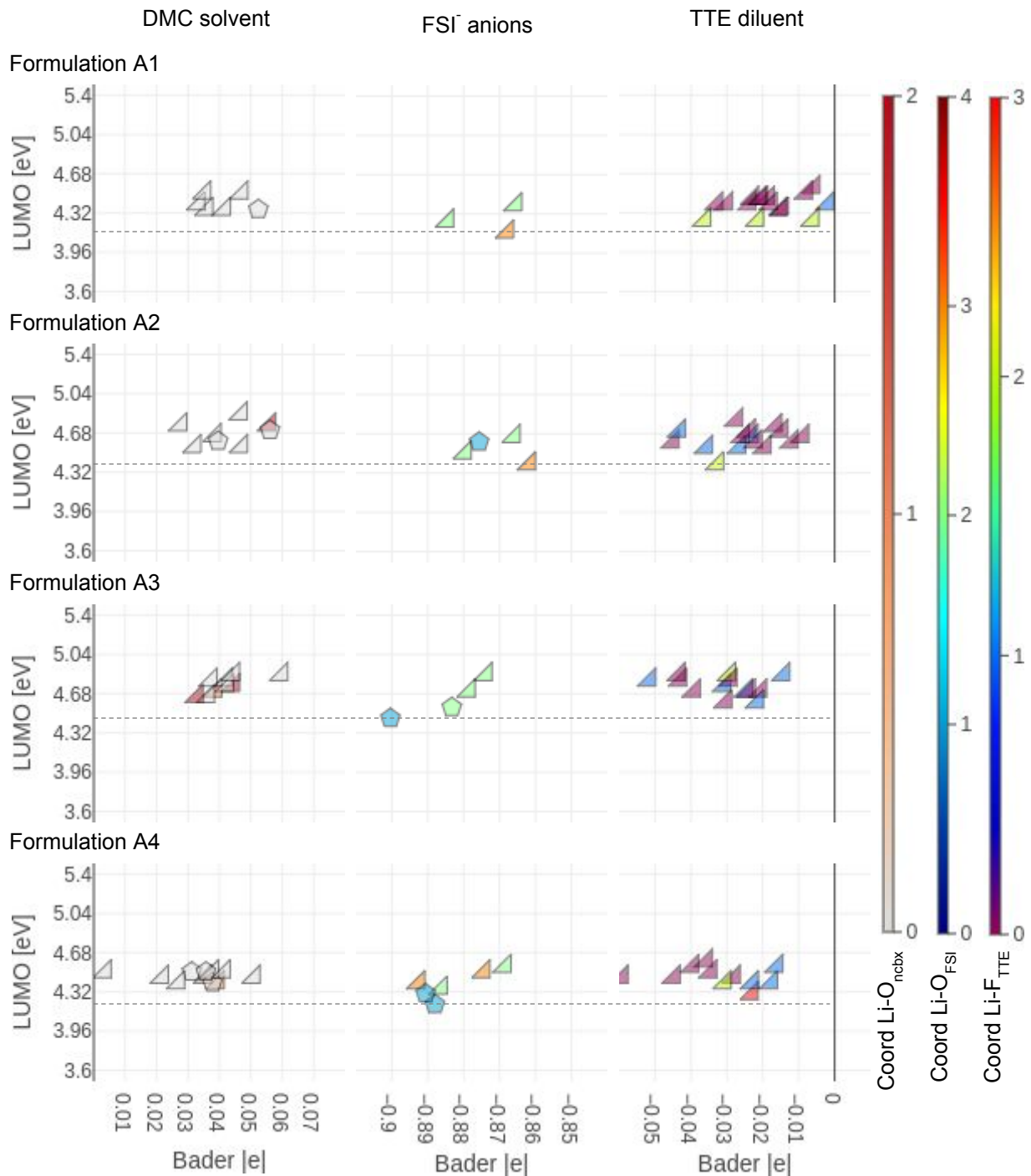


Figure 6: LUMO levels vs. bader electronic charges and Li-O, Li-F interactions for formulations A1, A2, A3, and A4.

Figure S2 outlines a similar analysis to elucidate changes in the electrolyte oxidative behavior based on the diluent contents. The DMC molecules score high HOMO levels in all formulations regardless of the diluent content. This behavior deviates from our earlier observations for HCE electrolytes with the same LiFSI:DMC molar ratio, where DMC coordination with Li^+ lowered HOMO levels down to the same level and even lower than FSI^- anions.¹² The TTE- Li^+ interaction via F atoms explains this deviation from the HCE formulation. Both TTE and DMC compete to interact with Li^+ , leading to an increase in the ratio of temporary non-associated DMC molecules even though the elevated LiFSI concentration. The TTE molecules engaged with Li^+ via one or two F atoms tend to lower their HOMO level. However, on average, non-associated TTE molecules score higher HOMO levels than FSI^- anions, which suggest an increased likelihood for these TTE molecules to oxidize on the cathode surface at high voltages to grow LiF-dominated passivation layers.^{3, 7} This behavior agrees with other studies on LHCE electrolytes using TTE as diluent for HCE electrolytes made from LiFSI and 1,2-dimethoxyethane (DME).³ The addition of TTE as diluent lowers the electrolyte viscosity, improves wettability, and enhances the stability of Ni-rich NMC811 cathodes under high potentials. X-ray photoelectron spectroscopy measurements indicate TTE participates in the cathode electrolyte interphase (CEI) formation. Figure S3 summarizes the reduction potential (vs. Li/Li^+) for all molecules and FSI^- anions with the geometry configurations and coordination with both Li^+ ions and F atoms adopted in formulations A1 to A4 in the same format used in Figure 6 and Figure S2. The reduction potential (in V) was calculated as the negative of the energy difference for the reaction $\text{A} + \text{e}^- \rightarrow \text{A}^-$, where A was the selected molecule in its respective environment, and A^- was the same configuration with an electron added. Reduction potentials in Figure S3 were normalized with respect to the potential for the reaction $\text{Li}^+ + \text{e}^- \rightarrow \text{Li}^0$, 1.37 V, obtained from Tables of Reduction Potentials. Figure S3 shows the dramatic impact that coordination with Li^+ ions has on the reduction potentials. The higher the coordination (shown by the color code in the figure), the easier the solvent molecules or FSI^- anions to reduce. It also shows how the TTE content modulates the overall FSI^- reduction behavior, the lower the diluent content, the FSI^- anions become easier to be reduced compared to both solvent and diluent. Finally, the Li^+ -F coordination also influences the TTE reduction behavior; TTE molecules engaged in Li^+ -F interactions are easier to reduce than uncoordinated TTE molecules.

Classical Molecular Dynamics Calculations

Classical MD simulations address the Li^+ transport mechanism of the LHCE electrolyte. We first run a first set of simulations without an electric field to verify the accuracy of the force field parameterization against the AIMD-NVT simulations and then add the electric field driving the Li^+ ions throughout the liquid structure. Table S1 specifies the number of molecules packed and cell dimensions used to verify the force field parameterization. The input geometries come from replicating the output geometries from AIMD-NVT simulations, such as the average number of particles per simulation cell increases close to three thousand atoms. The equilibration and production runs last for about 500 and 1000 ps, respectively.

We first compare in Figure S1 the Li-O and Li-F PRDF profiles with AIMD-NVT calculations. The Li-O interaction averages at 1.92 and 1.79 Å across all formulations for the AIMD-NVT and classical MD calculations, respectively, whereas the Li-F does it at 2.05 and 1.99 Å, respectively. This close agreement between both methods provides confidence in the force field's ability to handle intra- and inter-molecular interactions of the electrolyte liquid phase. Besides, no PRDF profile shows sharp peaks at long-range distances, suggesting no long-range ordering or salt crystallization regardless of the liquid phase's heterogeneities due to aggregate's formation.

As with Figure 2, Figure 7 displays the coordination number and the individual contributions to the solvation shell for each Li^+ averaged over the last 100 ps of simulation in high-diluent formulation A1. Like the AIMD-NVT simulation, the coordination number oscillates around 4.0 to 5.0 atoms with sulfonyl oxygen atoms from FSI⁻ anions and F atoms from TTE molecules contributing the most to complete the coordination sphere. DMC molecules contribute less to the solvation shell, and we attribute it to the presence of the TTE molecules. As with AIMD-NVT simulations, FSI⁻ anions do not interact with Li^+ via F atoms.

Figure S4 compares the aggregated structures from AIMD-NVT and classical MD in the liquid electrolyte for all formulations. Regardless of the simulation method, lowering the TTE content increases the size of the aggregated structures. The similarities between these two simulation methods in both the Li^+ coordination behavior and the aggregated structures' structural features give confidence in the force field parameterization ability to model the liquid electrolyte.

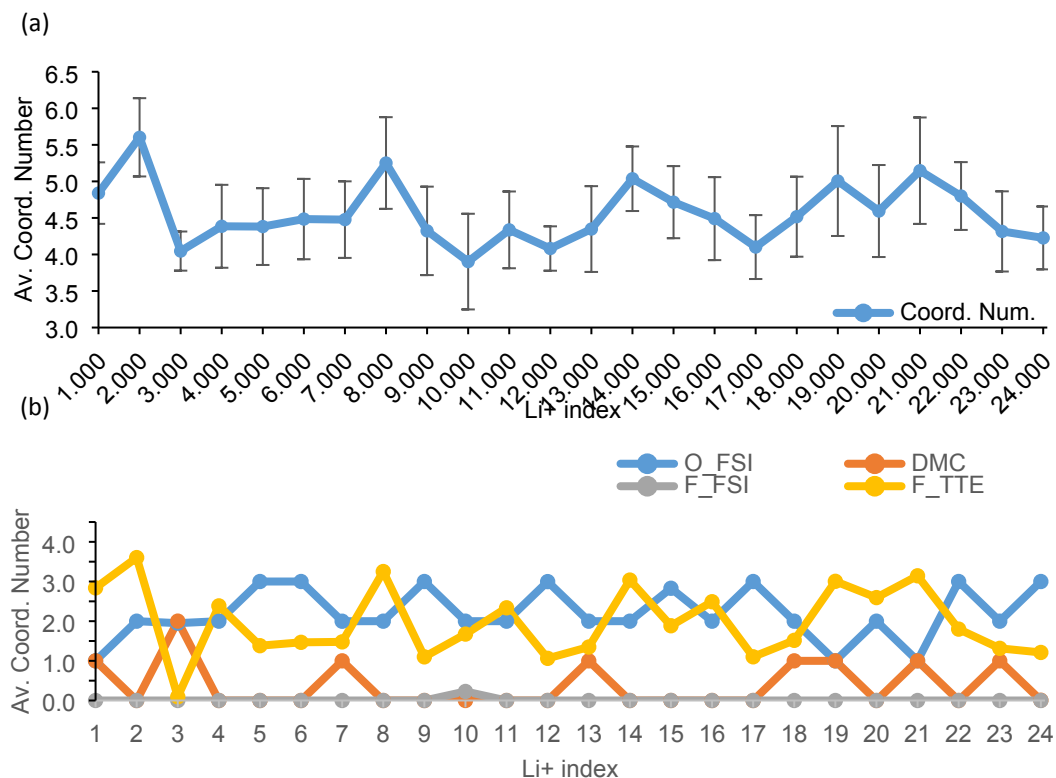


Figure 7: Li⁺ coordination behavior from classical MD simulations in formulation A1: (a) global coordination number, (b) species contribution to the Li⁺ coordination number. Bottom plot with no error bars for easier visualization purposes.

In regular battery operation, the electric field drives Li⁺ drifting motion throughout the electrolyte liquid structure. To set up the input geometries for this set of simulations, we take the output geometries from the classical MD simulations without electric field and replicate them along the electric field's direction. No simulation cell is shorter than 99.5 Å, long enough to follow the Li⁺ drifting motion. Table S2 shows the specifications for these simulation cells. We break periodicity along the z-coordinate and run a further equilibration job for 500 ps at 330 K with the NVT ensemble before activating the electric field. Afterward, we apply the electric field and let the calculation run for no less than 1.67 ns.

Figure 8 shows the simulation setup for formulation A1. The grey-colored polyhedral construction highlights the aggregated liquid structure without showing solvent and diluent molecules not associated with the aggregated. To keep the simulation cell neutral, we define reservoir and sink boxes on the left/right sides of the simulation cell to insert/remove Li⁺ ions once any Li⁺ ion reaches the end wall. The electric field equals 0.4 V/Å, and we keep it constant for all formulations. Even though this magnitude overwhelms any operational battery condition

from experiments, it allows us to observe the Li^+ drift displacement within the time simulation window still without triggering significant polarization effects in the liquid electrolyte.

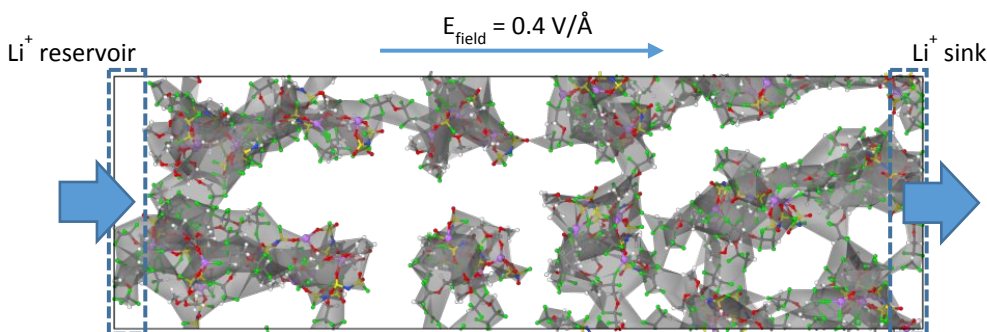


Figure 8: Simulation setup for evaluating Li^+ drifting displacement under external electric field. Grey colored polyhedral construction drans around the interconnected solvation shells. Non-associated solvent and diluent molecules not shown for easier visualization purposes.

Figure 9 shows the initial and final frames of the simulation cell for formulation A1. Even though the configuration of the aggregated structures changes, the concentration profiles plotted below each frame for Li^+ ions, FSI^- anions, and DMC and TTE molecules show no evidence of concentration polarization, as we observe no spatial separation between Li^+ ions and FSI^- anions even after 1.8 ns of simulation. The DMC and TTE molecules also show a concentration profile well spread throughout the simulation cell. The concentration profiles plotted in Figure S5 show the same behavior for formulations A2, A3, and A4, even though the incrementally lower diluent content from A2 to A4.

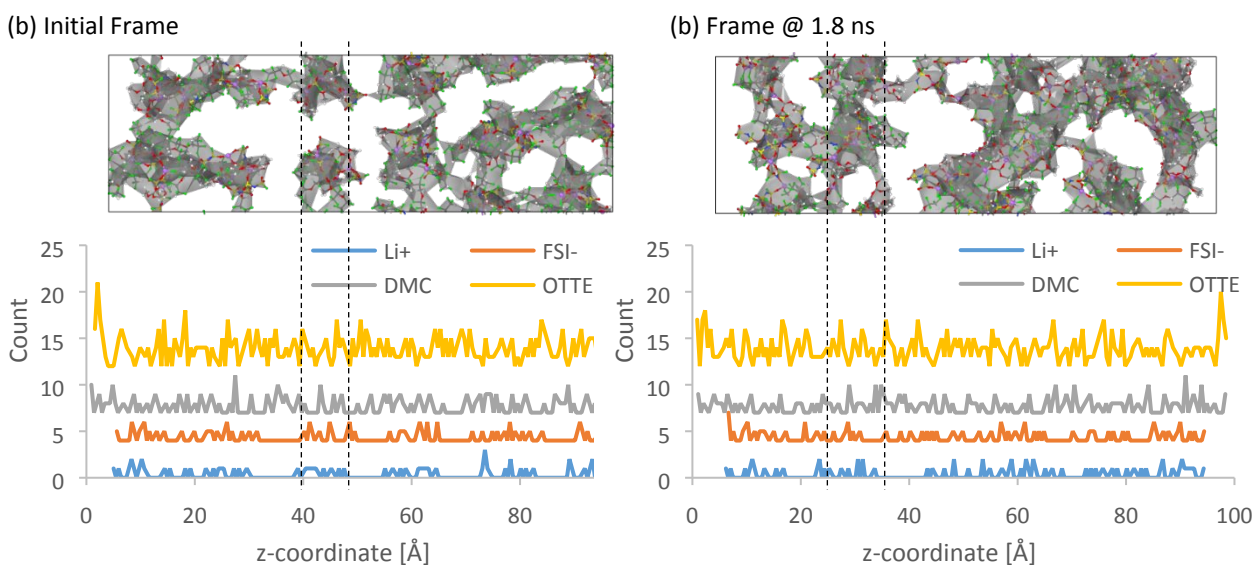


Figure 9: Concentration profiles in formulation A1 before (a) and after electric field applied (b).

Figure 10 summarizes the drift displacement under the electric field's influence for one Li^+ ion in formulation A1. The top left-sided plot follows the ion location along the electric field's direction vs. time. Meanwhile, the plots (b) and (c) correlate the drift displacement to the solvation shell coordination. The images on the right show the ion's solvation shell at selected frames. Even though the global coordination number averages at 4.24, the number of sulfonyl oxygen atoms from FSI⁻ anions changes with time, and the same do the number of carbonyl and ester oxygen atoms from DMC molecules, and F atoms from TTE molecules. Changes in the type of species involved in the solvation shell determine the drifting ion dynamics. Before 190 ps, two sulfonyl oxygen atoms, one carbonyl oxygen atom, and one F atom complete the solvation shell. Between 190 to 480 ps, the solvation shell changes to one sulfonyl oxygen atom, one carbonyl oxygen atom, and two F atoms. From 480 to 500 ps approximately (where the z coordinate shows a significant change), only F atoms surround the Li^+ ion. After 500 ps, sulfonyl oxygen atoms replace some F atoms, such as the species completing the solvation shell are FSI⁻ anions and TTE molecules. The Li^+ drifts slower whenever sulfonyl oxygen or carbonyl oxygen atoms dominate the solvation shell. Conversely, the Li^+ drifts faster if F atoms replace oxygen atoms.

This drifting behavior suggests that Li^+ ions exchange ligands dynamically via repeated ion dissociation/association, leading to a hopping conduction mechanism that conventional models such as the Onsager's theory and the Stoke's law cannot explain.^{9, 16, 22} Unexpectedly, TTE molecules act as fast conduction paths; Li^+ ions jump between aggregated networks built mainly from FSI⁻ anions via TTE diluent zones. The external electric field breaks Li-O interactions. The aggregated structure hinders displacement of individual FSI⁻ anions, and the weaker Li-F interactions, compared to Li-O (Figure 1 (c)), trigger faster Li^+ displacement between agglomerated clusters.

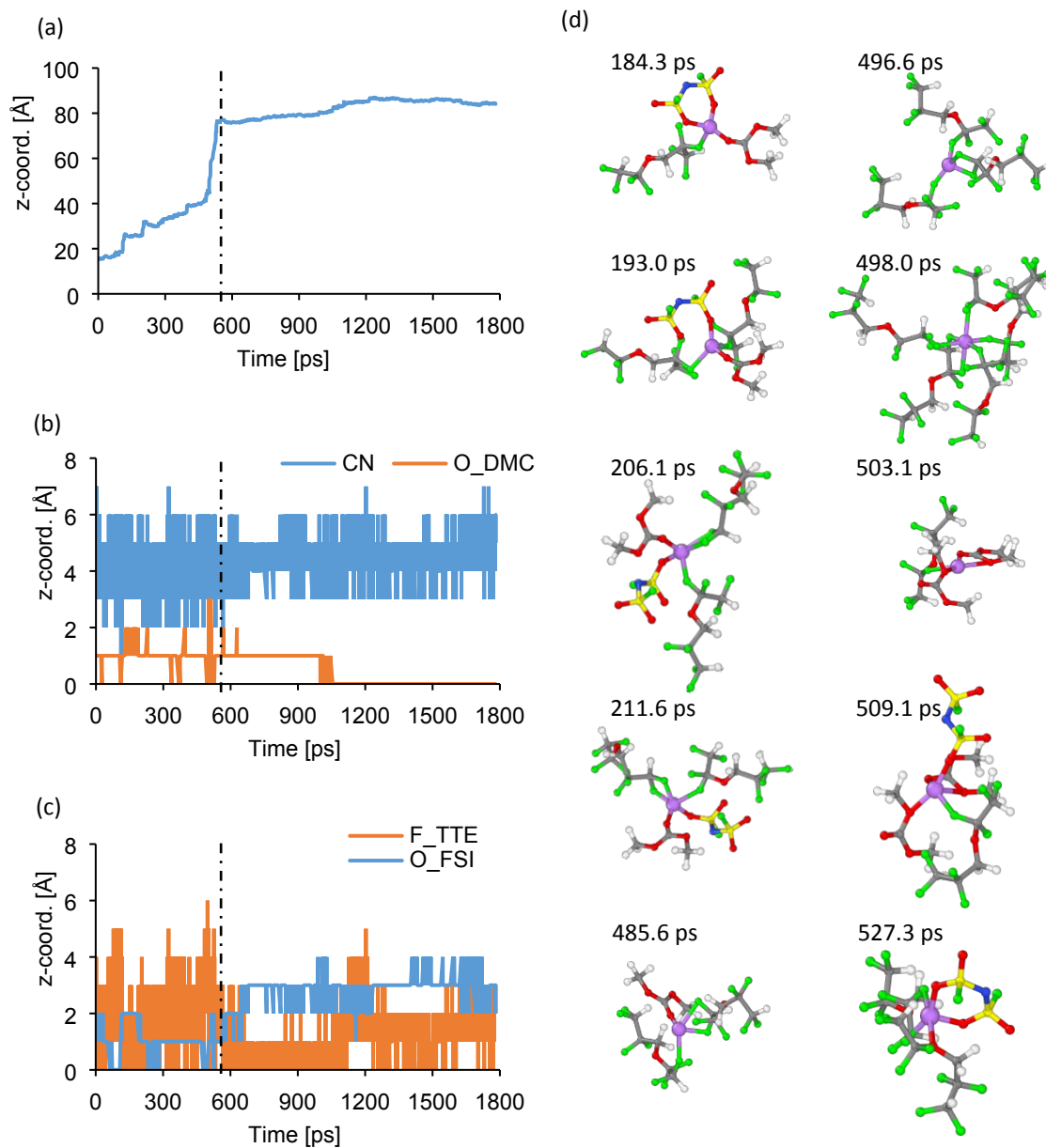


Figure 10: Drifting motion for one Li^+ in formulation A1 under influence of the electric field. (a) Li^+ location along the electric field direction vs. simulation time, (b) global coordination number (CN) and Li^+ coordination with DMC molecules (O_DMC), (c) Li^+ coordination with TTE molecules (F_TTE) and FSI $^-$ anions (O_FSI), (d) Li^+ solvation shell at selected times throughout the simulation.

For clarity, Figure 10 shows results just for one Li^+ ion; however we carefully checked the transport mechanisms for all other ions, and observed that this is the predominant ion dynamics throughout the simulation.

Figure 11 shows the average drift velocity for Li^+ ions, FSI $^-$ anions, and DMC and TTE molecules calculated using Equation 1; z_{end} and z_{initial} correspond to the end and initial

positions along the electric field's directions, evaluated at the t_{end} and t_{initial} times, respectively. The number of species packed in the simulation cell is n .

$$\langle v_{\text{drift}} \rangle = \frac{1}{n} \sum_{i=1}^n \left\{ \frac{z_{\text{end}} - z_{\text{initial}}}{t_{\text{end}} - t_{\text{initial}}} \right\}$$

Equation 1: Average drift velocity along the electric field direction

The external electric field ensures an average drift velocity for Li^+ ions positive along the electric field direction. However, this drift velocity slightly decreases with lower diluent contents. We attribute this behavior to a longer residence time of Li^+ ions in the aggregated liquid structures where Li^+ predominantly engages in stronger Li-O interactions compared to Li-F, which correlates with the increase in viscosity lowering the diluent content. LHCE electrolytes always lower viscosity after dilution and also usually lead to better ionic conductivity than equivalent HCE formulations unless too much diluent is added.⁶ Besides, with lower diluent contents, fewer TTE molecules are available to provide fast conduction paths, as we discuss above. The FSI⁻ anions show a negative drift velocity but three to four orders of magnitude lower than Li^+ ions. This behavior suggests negligible concentration polarization, and the difference in magnitude indicates decoupled Li^+ and FSI⁻ dynamics. As with the structural transport mechanism,¹⁶ these uncorrelated drift velocities, indicate that neighboring species do not diffuse together by any appreciable amount. Besides, the ability of Li^+ to drift via repeated hopping events hinders concentration polarization, favoring increased limiting current density and improved rate capability, compared to conventional diluted electrolytes.¹⁶ The average drift velocities for DMC and TTE molecules do not show evident changes based on the diluent content and are four to five orders of magnitude lower than Li^+ ions, indicating decoupled dynamics even though the interaction with Li^+ via carbonyl oxygen and F atoms, respectively.

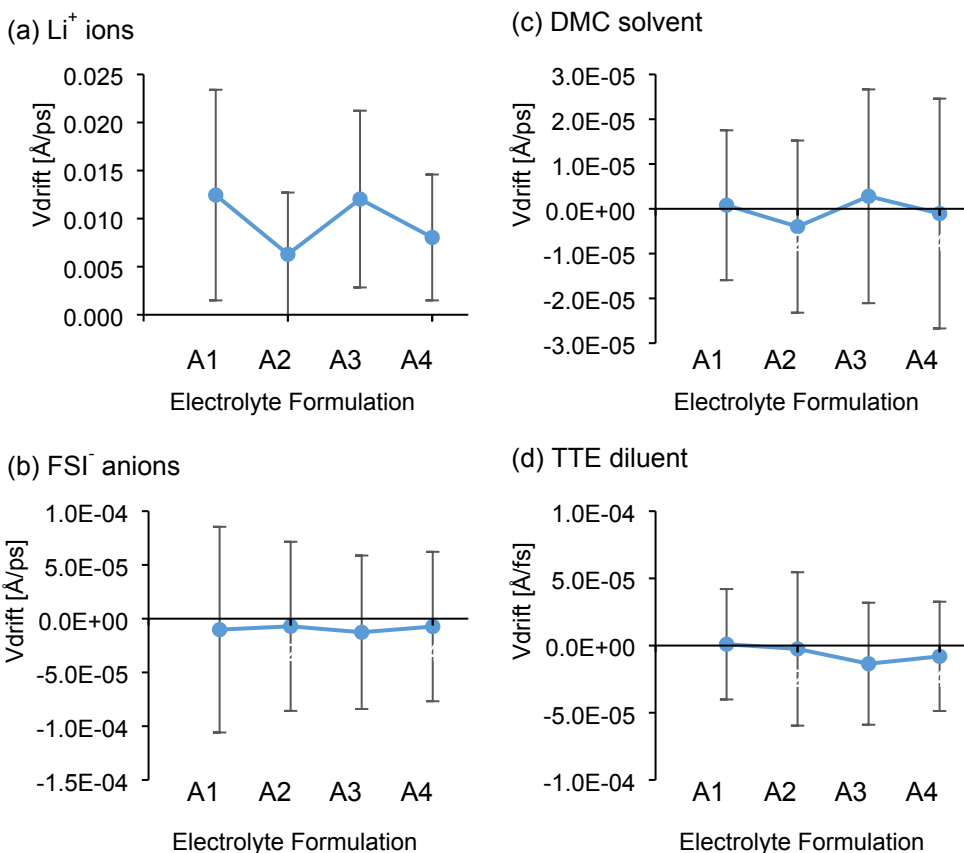


Figure 11: Averaged drift velocities under influence of electric field for: (a) Li^+ ions, (b) FSI^- anions, (c) DMC solvent, and (d) TTE diluent

Figure 12 summarizes every possible solvation shell for all Li^+ ions at every step of the simulation for high diluent formulation A1, calculating the average displacement between two consecutive frames in the atomic trajectory for each combination and counting how many times each of these combinations repeat.

The most common coordination shell has four surrounding atoms, two sulfonyl oxygen atoms from FSI^- anions, one carbonyl oxygen atom from DMC molecules, and one F atom from TTE molecules. The second most repeated one has five atoms completing the solvation shell with three oxygen atoms from FSI^- anions and two F atoms from TTE molecules. The third one has one oxygen atom from FSI^- anions and two F atoms from TTE molecules. Every saved frame in the simulation separates apart 0.125 ps, and the most significant displacement along the electric field for this time interval averages close to 0.6 \AA . The solvation shell ranking this average displacement has one carbonyl oxygen atom and two F atoms. The solvation shell with the second-largest displacement has one sulfonyl oxygen atom and three F atoms, while the third one has one carbonyl oxygen atoms and three F atoms. Solvation shells with one, two,

three and even four F atoms show the larger displacements but quickly become less common as the number of F atoms increases. Moreover, solvation shells with more than two sulfonyl oxygen atoms quickly become less common and show shorter average displacements.

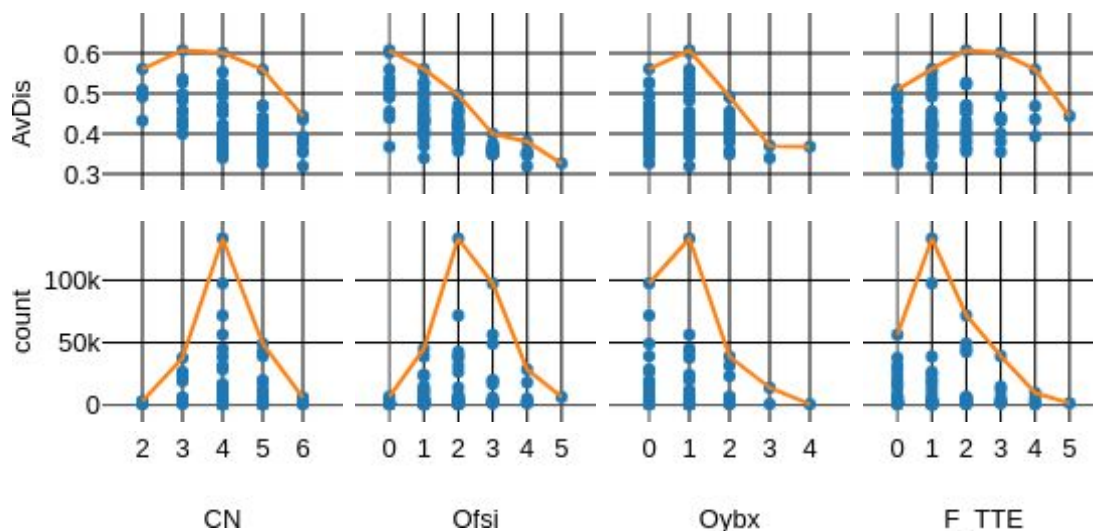


Figure 12: Solvation shells computed in formulation A1 for all Li^+ ions for every step of the simulation: Average Li^+ displacement between two consecutive frames (0.125 ps) and number of times the solvation shells repeats throughout the simulation (count) vs. global coordination number (CN), Li^+ coordination with FSI^- anions (Ofsi), carbonyl oxygen atoms (Oybx), and TTE molecules (F_TTE)

Figures S6, S7, and S8 summarize the same coordination analysis for formulations A2, A3, and A4. The most common solvation shells have four to five atoms in all formulations with TTE and DMC molecules competitively interacting with Li^+ regardless of the diluent content. The number of sulfonyl oxygen atoms completing the most common solvation shells increases from two to three atoms with lower diluent contents proper of the electrolyte's increased aggregation state. Similarly, the number of F atoms from TTE molecules for the most common solvation shells decreases with lower diluent content proper of the less availability of TTE molecules.

Conclusions

This work shows that TTE interacts with Li^+ ions with F atoms instead of ether oxygen atoms. The proportion of TTE molecules coordinating Li^+ via one or two F atoms increases with lower diluent contents. As with the equivalent HCE, high salt concentration leads to the formation of aggregates. The FSI^- anions direct these aggregated structures' structural features due to the availability of multiple sulfonyl oxygen atoms and the anion structural flexibility that can adopt multiple configurations. All FSI^- anions coordinate with Li^+ regardless of the diluent content.

FSI⁻ anions score lower LUMO levels regardless of the diluent content, making the Li salt more likely to be reduced and contribute to more stable passivation layers on negative electrodes. Free diluent molecules are more likely to oxidize at high potentials, contributing to LiF concentrated passivation films on cathode electrolytes that potentially enhance the electrochemical battery performance.

Li⁺ ions drift throughout the liquid structure via repeated ion dissociation/association processes that lead to a hopping conduction mechanism in which the nature of the solvation shell continuously changes throughout the drifting motion. Li⁺ ions interact with TTE molecules via F atoms and eventually jump between aggregated networks where Li-O interactions dominate, via diluent-enriched phases, such as the solvation shell temporarily mutating to a Li-F coordination structure. The weaker Li-F interaction makes the drifting displacement faster until the Li⁺ ions engage with Li-O interactions again. Our results contribute to a better atomic-level understanding of the liquid structure of LHCE electrolytes and provide pathways to efficient dilution strategies for HCE electrolytes.

Author contributions

All authors have given approval to the final version of the manuscript. S.P.B. performed all the computations and analyzed the outputs from first-principles simulations. P.B.B. originated the idea, and supervised the work. X.C., P.Z.E-K, and J-G. Z. performed the Raman experiments and analyses. S.P.B. and P.B. B. discussed and interpreted the results together with X.C. and J-G.Z., and contributed to the preparation of the manuscript.

Conflicts of Interest

There are no conflicts of interest to declare.

Acknowledgements

This material is based upon work supported by the U.S. Department of Energy's Office of Energy Efficiency and Renewable Energy (EERE), as part of the Battery 500 Consortium, Award Number DE-EE0008210. X. Cao and J.G. Zhang are supported by the Assistant Secretary for Energy Efficiency and Renewable Energy (EERE), Vehicle Technologies Office (VTO), of the U.S. Department of Energy (DOE) through the Advanced Battery Materials Research (BMR) program (Battery500 Consortium) under contract no. DE-AC05-76RL01830.

Supercomputer resources from the Texas A&M University High Performance Computer Center and Texas Advanced Computing Center (TACC) are gratefully acknowledged.

Supporting Information

The following materials are available: Simulation cell size, number of molecules, and molar ratios for each formulation for simulations with and without electric field (Tables S1 and S2); Comparison of PRDFs from classical and ab initio simulations (Figure S1); HOMO levels and Bader electronic charges for all formulations (Figure S2); Absolute Reduction Potential vs. Bader electronic charges and Li-O, Li-F interactions for formulations A1, A2, A3, and A4 (Figure S3); Comparison of solution structure from AIMD and classical MD (Figure S4); Concentration profiles before and after applying electric field (0.4 V/Å): Formulations A1, A3, and A4 (Figure S5); Coordination profiles for formulations A2, A3, and A4 (Figures S6, S7, and S8).

References

1. Liu, J.; Bao, Z.; Cui, Y.; Dufek, E. J.; Goodenough, J. B.; Khalifah, P.; Li, Q.; Liaw, B. Y.; Liu, P.; Manthiram, A.; Meng, Y. S.; Subramanian, V. R.; Toney, M. F.; Viswanathan, V. V.; Whittingham, M. S.; Xiao, J.; Xu, W.; Yang, J.; Yang, X.-Q.; Zhang, J.-G., Pathways for Practical High-Energy Long-Cycling Lithium Metal Batteries. *Nat. Energy* **2019**, *4* (3), 180-186.
2. Dolotko, O.; Senyshyn, A.; Mühlbauer, M.; Nikolowski, K.; Ehrenberg, H., Understanding Structural Changes in NMC Li-Ion Cells by In Situ Neutron Diffraction. *J. Power Sources* **2014**, *255*, 197-203.
3. Ren, X.; Zou, L.; Cao, X.; Engelhard, M. H.; Liu, W.; Burton, S. D.; Lee, H.; Niu, C.; Matthews, B. E.; Zhu, Z.; Wang, C.; Arey, B. W.; Xiao, J.; Liu, J.; Zhang, J.-G.; Xu, W., Enabling High-Voltage Lithium-Metal Batteries Under Practical Conditions. *Joule* **2019**, *3* (7), 1662-1676.
4. Lin, F.; Markus, I. M.; Nordlund, D.; Weng, T.-C.; Asta, M. D.; Xin, H. L.; Doeff, M. M., Surface Reconstruction and Chemical Evolution of Stoichiometric Layered Cathode Materials for Lithium-Ion Batteries. *Nat. Commun.* **2014**, *5*, 3529.
5. Yamada, Y.; Yamada, A., Review—Superconcentrated Electrolytes for Lithium Batteries. *J. Electrochem. Soc.* **2015**, *162* (14), A2406-A2423.
6. Chen, S.; Zheng, J.; Mei, D.; Han, K. S.; Engelhard, M. H.; Zhao, W.; Xu, W.; Liu, J.; Zhang, J.-G., High-Voltage Lithium-Metal Batteries Enabled by Localized High-Concentration Electrolytes. *Adv. Mater.* **2018**, *30* (21), 1706102.
7. Zhang, X.; Zou, L.; Xu, Y.; Cao, X.; Engelhard, M. H.; Matthews, B. E.; Zhong, L.; Wu, H.; Jia, H.; Ren, X.; Gao, P.; Chen, Z.; Qin, Y.; Kompella, C.; Arey, B. W.; Li, J.; Wang, D.; Wang, C.; Zhang, J.-G.; Xu, W., Advanced Electrolytes for Fast-Charging High-Voltage Lithium-Ion Batteries in Wide-Temperature Range. *Adv. Energy Mater.* **2020**, *10* (22), 2000368.

8. Nilsson, V.; Bernin, D.; Brandell, D.; Edström, K.; Johansson, P., Interactions and Transport in Highly Concentrated LiTFSI-based Electrolytes. *ChemPhysChem* **21** (11), 1166-1176.
9. Yamada, Y.; Wang, J.; Ko, S.; Watanabe, E.; Yamada, A., Advances and Issues in Developing Salt-Concentrated Battery Electrolytes. *Nat. Energy* **2019**, *4* (4), 269-280.
10. Jie, Y.; Ren, X.; Cao, R.; Cai, W.; Jiao, S., Advanced Liquid Electrolytes for Rechargeable Li Metal Batteries. *Adv. Funct. Mater.* **2020**, *30* (25), 1910777.
11. Wang, J.; Yamada, Y.; Sodeyama, K.; Chiang, C. H.; Tateyama, Y.; Yamada, A., Superconcentrated Electrolytes for a High-Voltage Lithium-Ion Battery. *Nat. Commun.* **2016**, *7* (1), 12032.
12. Perez Beltran, S.; Cao, X.; Zhang, J.-G.; Balbuena, P. B., Localized High Concentration Electrolytes for High Voltage Lithium-Metal Batteries: Correlation between the Electrolyte Composition and its Reductive/Oxidative Stability. *Chem. Mater.* **2020**, *32* (14), 5973–5984.
13. Ren, X.; Chen, S.; Lee, H.; Mei, D.; Engelhard, M. H.; Burton, S. D.; Zhao, W.; Zheng, J.; Li, Q.; Ding, M. S.; Schroeder, M.; Alvarado, J.; Xu, K.; Meng, Y. S.; Liu, J.; Zhang, J.-G.; Xu, W., Localized High-Concentration Sulfone Electrolytes for High-Efficiency Lithium-Metal Batteries. *Chem* **2018**, *4* (8), 1877-1892.
14. Lee, Y.; Lee, T. K.; Kim, S.; Lee, J.; Ahn, Y.; Kim, K.; Ma, H.; Park, G.; Lee, S.-M.; Kwak, S. K.; Choi, N.-S., Fluorine-Incorporated Interface Enhances Cycling Stability of Lithium Metal Batteries with Ni-rich NCM Cathodes. *Nano Energy* **2020**, *67*, 104309.
15. Ren, X.; Xu, W.; Zhang, J.-g., High Efficiency Electrolytes for High Voltage Battery Systems. US Patent App. 16/230,531: 2019.
16. Self, J.; Fong, K. D.; Persson, K. A., Transport in Superconcentrated LiPF₆ and LiBF₄/Propylene Carbonate Electrolytes. *ACS Energy Lett.* **2019**, *4* (12), 2843-2849.
17. Manthiram, A.; Yu, X.; Wang, S., Lithium Battery Chemistries Enabled by Solid-State Electrolytes. *Nat. Rev. Mater.* **2017**, *2* (4), 16103.
18. Shi, S.; Lu, P.; Liu, Z.; Qi, Y.; Hector, L. G.; Li, H.; Harris, S. J., Direct Calculation of Li-Ion Transport in the Solid Electrolyte Interphase. *J. Am. Chem. Soc.* **2012**, *134* (37), 15476-15487.
19. Zhang, Z.; Zou, Z.; Kaup, K.; Xiao, R.; Shi, S.; Avdeev, M.; Hu, Y.-S.; Wang, D.; He, B.; Li, H.; Huang, X.; Nazar, L. F.; Chen, L., Correlated Migration Invokes Higher Na⁺-Ion Conductivity in NaSICON-Type Solid Electrolytes. *Adv. Energy Mater.* **2019**, *9* (42), 1902373.
20. Zou, Z.; Ma, N.; Wang, A.; Ran, Y.; Song, T.; Jiao, Y.; Liu, J.; Zhou, H.; Shi, W.; He, B.; Wang, D.; Li, Y.; Avdeev, M.; Shi, S., Relationships Between Na⁺ Distribution, Concerted Migration, and Diffusion Properties in Rhombohedral NASICON. *Adv. Energy Mater.* **2020**, *10* (30), 2001486.
21. Åvall, G.; Johansson, P., A Novel Approach to Ligand-Exchange Rates Applied to Lithium-Ion Battery and Sodium-Ion Battery Electrolytes. *J. Chem. Phys.* **2020**, *152* (23), 234104.
22. Dokko, K.; Watanabe, D.; Ugata, Y.; Thomas, M. L.; Tsuzuki, S.; Shinoda, W.; Hashimoto, K.; Ueno, K.; Umebayashi, Y.; Watanabe, M., Direct Evidence for Li Ion

- Hopping Conduction in Highly Concentrated Sulfolane-Based Liquid Electrolytes. *J. Phys. Chem. B* **2018**, *122* (47), 10736-10745.
23. Cao, X.; Zou, L.; Matthews, B. E.; Zhang, L.; He, X.; Ren, X.; Engelhard, M. H.; Burton, S. D.; El-Khoury, P. Z.; Lim, H.-S., Optimization of Fluorinated Orthoformate Based Electrolytes for Practical High-Voltage Lithium Metal Batteries. *Energy Storage Mater.* **2020**, *34*, 76-84
24. Kresse, G.; Hafner, J., Ab Initio Molecular-Dynamics Simulation of the Liquid-Metal--Amorphous-Semiconductor Transition in Germanium. *Phys. Rev. B* **1994**, *49* (20), 14251-14269.
25. Kresse, G.; Furthmüller, J., Efficient Iterative Schemes for Ab Initio Total-Energy Calculations Using a Plane-Wave Basis Set. *Phys. Rev. B* **1996**, *54* (16), 11169-11186.
26. Kresse, G.; Furthmüller, J., Efficiency of Ab-Initio Total Energy Calculations for Metals and Semiconductors Using a Plane-Wave Basis Set. *Comput. Mater. Sci.* **1996**, *6* (1), 15-50.
27. Parrinello, M.; Rahman, A., Crystal Structure and Pair Potentials: A Molecular-Dynamics Study. *Phys. Rev. Lett.* **1980**, *45* (14), 1196-1199.
28. Parrinello, M.; Rahman, A., Polymorphic Transitions in Single Crystals: A New Molecular Dynamics Method. *J. Appl. Phys.* **1981**, *52* (12), 7182-7190.
29. Burgos, J. C.; Balbuena, P. B.; Montoya, J. A., Structural Dependence of the Sulfur Reduction Mechanism in Carbon-Based Cathodes for Lithium–Sulfur Batteries. *J. Phys. Chem. C* **2017**, *121* (34), 18369-18377.
30. Nosé, S., A Unified Formulation of the Constant Temperature Molecular Dynamics Methods. *J. Chem. Phys.* **1984**, *81* (1), 511-519.
31. Hoover, W. G., Canonical Dynamics: Equilibrium Phase-Space Distributions. *Phys. Rev. A* **1985**, *31* (3), 1695-1697.
32. Frenkel, D.; Smit, B., Understanding Molecular Simulation 2nd Edition. Academic Press, London, UK: 2002.
33. Kamphaus, E. P.; Balbuena, P. B., First-Principles Investigation of Lithium Polysulfide Structure and Behavior in Solution. *J. Phys. Chem. C* **2017**, *121* (39), 21105-21117.
34. Kresse, G.; Joubert, D., From Ultrasoft Pseudopotentials to the Projector Augmented-Wave Method. *Phys. Rev. B* **1999**, *59* (3), 1758-1775.
35. Perdew, J. P.; Burke, K.; Ernzerhof, M., Generalized Gradient Approximation Made Simple. *Phys. Rev. Lett.* **1996**, *77* (18), 3865-3868.
36. Monkhorst, H. J.; Pack, J. D., Special Points for Brillouin-Zone Integrations. *Phys. Rev. B* **1976**, *13* (12), 5188-5192.
37. Dronskowski, R.; Bloechl, P. E., Crystal Orbital Hamilton Populations (COHP): Energy-Resolved Visualization of Chemical Bonding in Solids Based on Density-Functional Calculations. *J. Phys. Chem.* **1993**, *97* (33), 8617-8624.
38. Deringer, V. L.; Tchougréeff, A. L.; Dronskowski, R., Crystal Orbital Hamilton Population (COHP) Analysis as Projected From Plane-Wave Basis Sets. *J. Phys. Chem. A* **2011**, *115* (21), 5461-5466.
39. Maintz, S.; Deringer, V. L.; Tchougréeff, A. L.; Dronskowski, R., Analytic Projection From Plane-Wave and PAW Wavefunctions and Application to Chemical-Bonding Analysis in Solids. *J. Comput. Chem.* **2013**, *34* (29), 2557-2567.

40. Maintz, S.; Deringer, V. L.; Tchougréeff, A. L.; Dronskowski, R., LOBSTER: A tool to Extract Chemical Bonding From Plane-Wave Based DFT. *J. Comput. Chem.* **2016**, *37* (11), 1030-1035.
41. Deringer, V. L.; Zhang, W.; Lumeij, M.; Maintz, S.; Wuttig, M.; Mazzarello, R.; Dronskowski, R., Bonding Nature of Local Structural Motifs in Amorphous GeTe. *Angew. Chem., Int. Ed.* **2014**, *53* (40), 10817-10820.
42. Nelson, R.; Konze, P. M.; Dronskowski, R., First-Principles Chemical Bonding Study of Manganese Carbodiimide, MnNCN, As Compared to Manganese Oxide, MnO. *J. Phys. Chem. A* **2017**, *121* (40), 7778-7786.
43. Henkelman, G.; Arnaldsson, A.; Jónsson, H., A Fast and Robust Algorithm for Bader Decomposition of Charge Density. *Comput. Mater. Sci.* **2006**, *36* (3), 354-360.
44. Tang, W.; Sanville, E.; Henkelman, G., A Grid-Based Bader Analysis Algorithm Without Lattice Bias. *J. Phys.: Condens. Matter* **2009**, *21* (8), Article no. 084204.
45. Sanville, E.; Kenny, S. D.; Smith, R.; Henkelman, G., Improved Grid-Based Algorithm for Bader Charge Allocation. *J. Comput. Chem.* **2007**, *28* (5), 899-908.
46. Plimpton, S., Fast Parallel Algorithms for Short-Range Molecular Dynamics. *J. Comput. Phys.* **1995**, *117* (1), 1-19.
47. Humbert, M. T., *Classical Molecular Dynamics Simulations of Electrolyte Solutions for next Generation Batteries*. University of Notre Dame: 2019.
48. Canongia Lopes, J. N.; Shimizu, K.; Pádua, A. A. H.; Umehayashi, Y.; Fukuda, S.; Fujii, K.; Ishiguro, S.-i., Potential Energy Landscape of Bis(fluorosulfonyl)amide. *J. Phys. Chem. B* **2008**, *112* (31), 9449-9455.
49. Islam, M. M.; van Duin, A. C. T., Reductive Decomposition Reactions of Ethylene Carbonate by Explicit Electron Transfer from Lithium: An eReaxFF Molecular Dynamics Study. *J. Phys. Chem. C* **2016**, *120* (48), 27128-27134.
50. Soetens, J.-C.; Millot, C.; Maigret, B.; Bakó, I., Molecular Dynamics Simulation and X-Ray Diffraction Studies of Ethylene Carbonate, Propylene Carbonate and Dimethyl Carbonate in Liquid Phase. *J. Mol. Liq.* **2001**, *92* (3), 201-216.
51. Esser, M.; Esser, A. A.; Proserpio, D. M.; Dronskowski, R., Bonding Analyses of Unconventional Carbon Allotropes. *Carbon* **2017**, *121*, 154-162.
52. Piao, N.; Ji, X.; Xu, H.; Fan, X.; Chen, L.; Liu, S.; Garaga, M. N.; Greenbaum, S. G.; Wang, L.; Wang, C.; He, X., Countersolvent Electrolytes for Lithium-Metal Batteries. *Adv. Energy Mater.* **2020**, *10* (10), 1903568.
53. Hyodo, S.-A.; Okabayashi, K., Raman Intensity Study of Local Structure in Non-Aqueous Electrolyte Solutions—I. Cation-Solvent Interaction in LiClO₄/Ethylene Carbonate. *Electrochim. Acta* **1989**, *34* (11), 1551-1556.
54. Seo, D. M.; Boyle, P. D.; Borodin, O.; Henderson, W. A., Li⁺ Cation Coordination by Acetonitrile—Insights From Crystallography. *RSC Adv.* **2012**, *2* (21), 8014-8019.